The Cryosphere

Supplement of

Disentangling the drivers of future Antarctic ice loss with a historically calibrated ice-sheet model

Violaine Coulon et al.

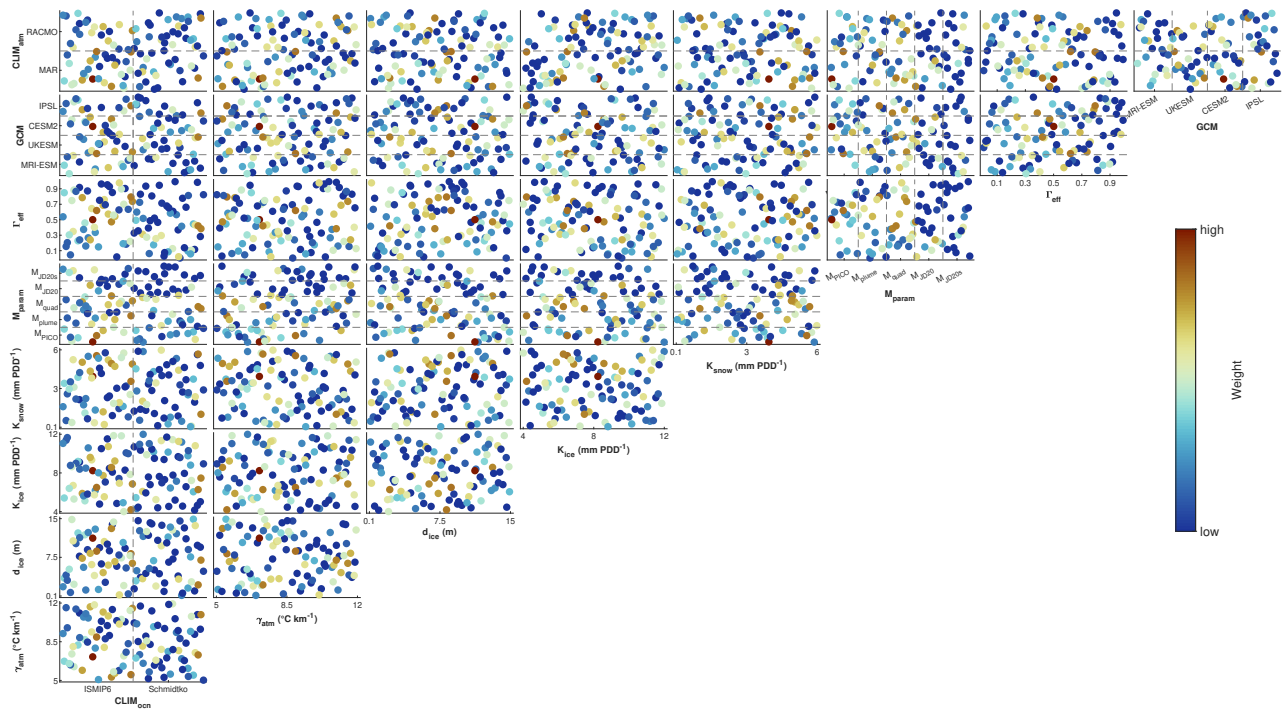*Correspondence to:* Violaine Coulon (violaine.coulon@ulb.be)

Figure S1: **Likelihood weight for the 100-members ensemble of simulations accounting for key uncertainties in ice-ocean and ice-atmosphere interactions over the 9-D parameter space**. The parameters are the atmospheric ($CLIM_{atm}$) and oceanic ($CLIM_{ocn}$) present-day climatologies, the applied sub-shelf melt parameterisation (M_{param}), the effective ice–ocean heat flux (Γ_{eff}), the positive degree-day (PDD) snow melt factor (K_{snow}), the PDD ice melt factor (K_{ice}), the thickness of the thermally-active layer (d_{ice}), the atmospheric lapse rate (γ_{atm}), and the applied GCM (GCM). Note that for the parameters characterised by discrete values, i.e., $CLIM_{atm}$, $CLIM_{ocn}$, M_{param}, and GCM, the continuous parameter space is divided into a finite number of equal probability regions, or bins, displayed by the dashed lines.
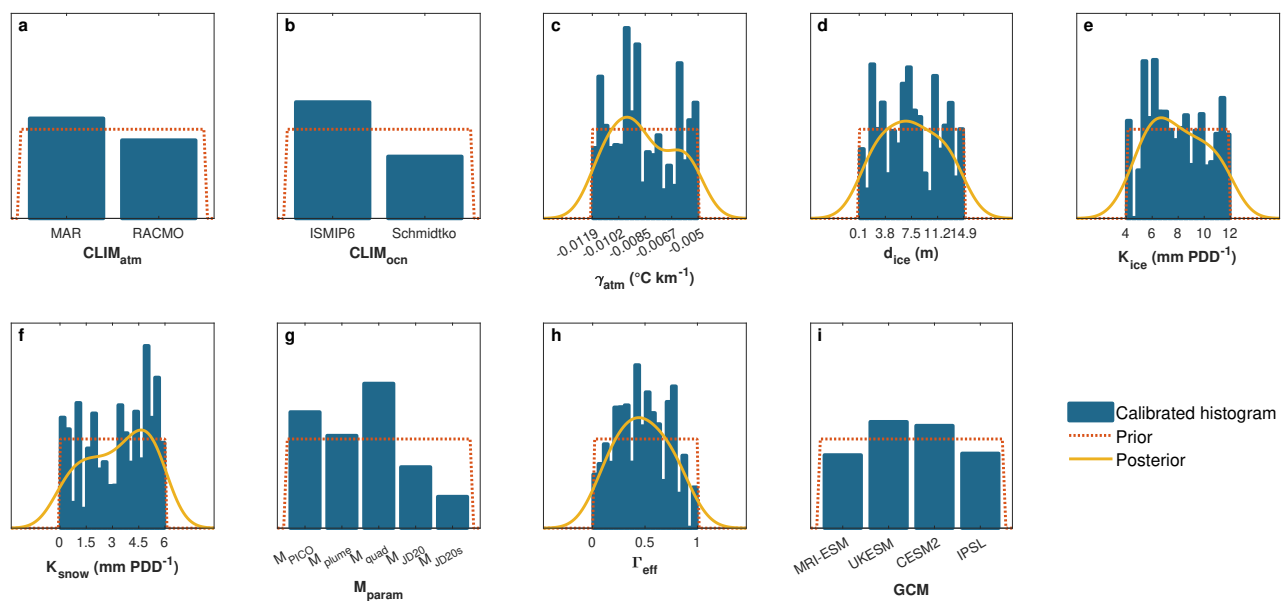
Figure S2: **Posterior parameter probability distributions and density histograms resulting from the calibration.** Posterior parameter density histograms and probability distribution functions approximated using kernel density estimation (lines) are shown for all parameters except discretely distributed parameters (CLIM$_{atm}$, CLIM$_{ocn}$, M_{param}, and GCM). The prior distributions are shown as dashed orange lines while the posterior distributions are shown as yellow lines. Weighted histograms are shown in blue.
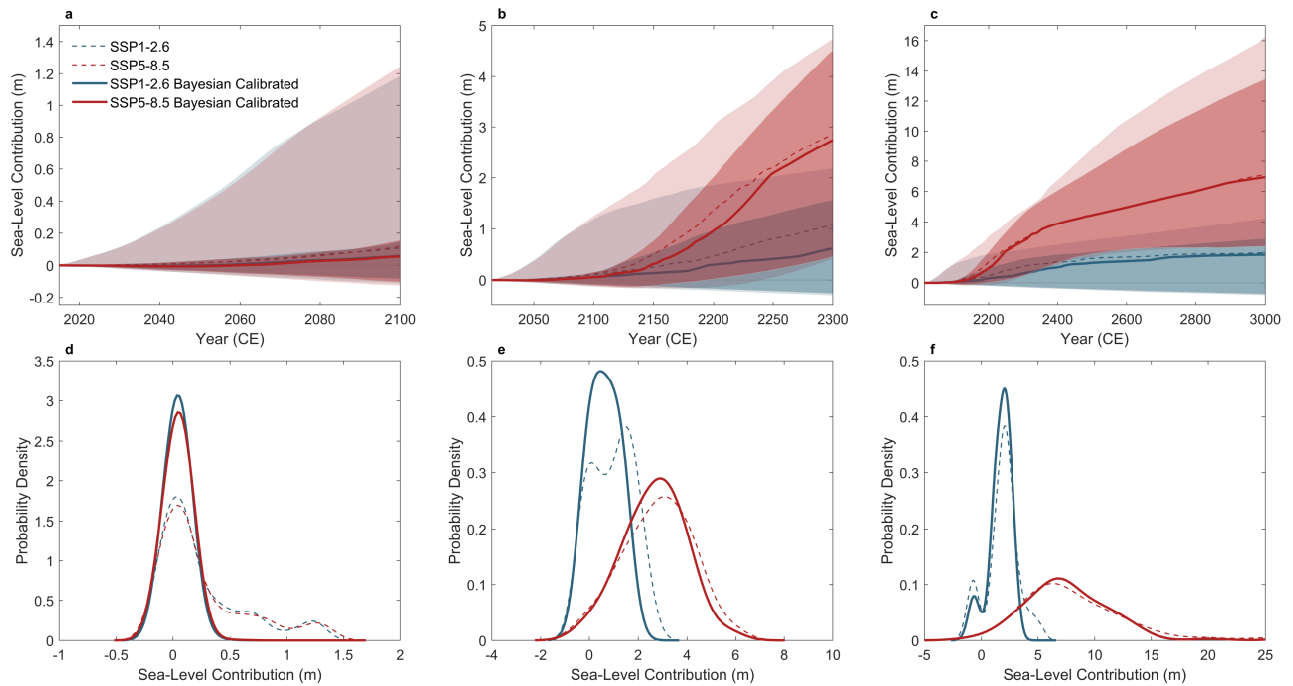
Figure S3: **Comparison of the prior and posterior distributions of projected Antarctic contribution to global mean sea-level rise until the end of the millennium.** Evolution of the ensemble projected contribution to sea-level from the Antarctic ice sheet until (a) 2100, (b) 2300, and (c) 3000 CE, under the Shared Socio-Economic Pathways (SSP) 1-2.6 and SSP5-8.5 scenarios (N=100 per SSP scenario). The ensemble uncalibrated median (dashed lines) and 5–95% probability interval (light dashed area) is compared to the Bayesian calibrated ensemble median (solid lines) and 5–95% probability interval (dark shaded area), with 5-year running average applied. d–f represent the prior (dashed lines) and posterior (solid lines) probability density functions of the sea-level contribution from the AIS for the years (d) 2100, (e) 2300 and (f) 3000 under SSP1-2.6 (blue lines) and SSP5-8.5 (red lines).
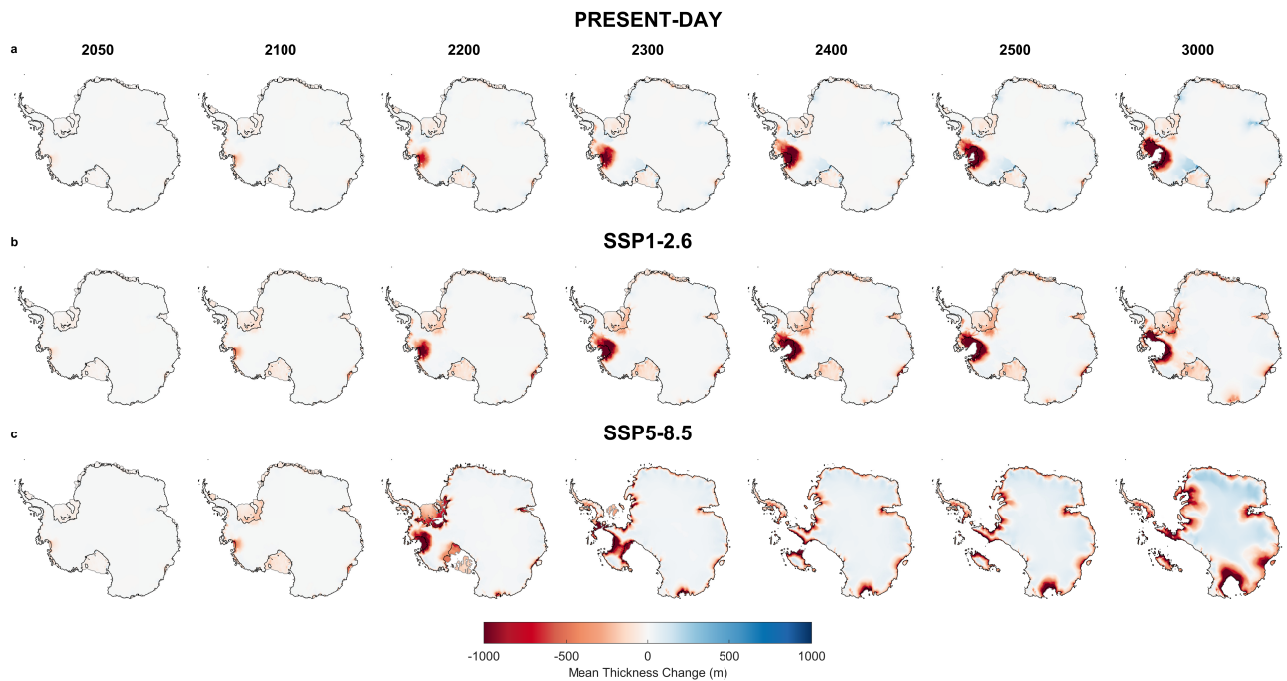
Figure S4: **Mean ice thickness change under (a) constant present-day climate conditions (PRESENT-DAY), shared socio-economic pathways (SSP) 1-2.6 (b) and 5-8.5 (c) at different points in time throughout the millennia.** For each scenario, the mean thickness change at a given point is computed using the Bayesian calibrated mean of the ensemble (N=100). Black and grey lines show the ensemble mean grounding line and calving front positions, respectively.
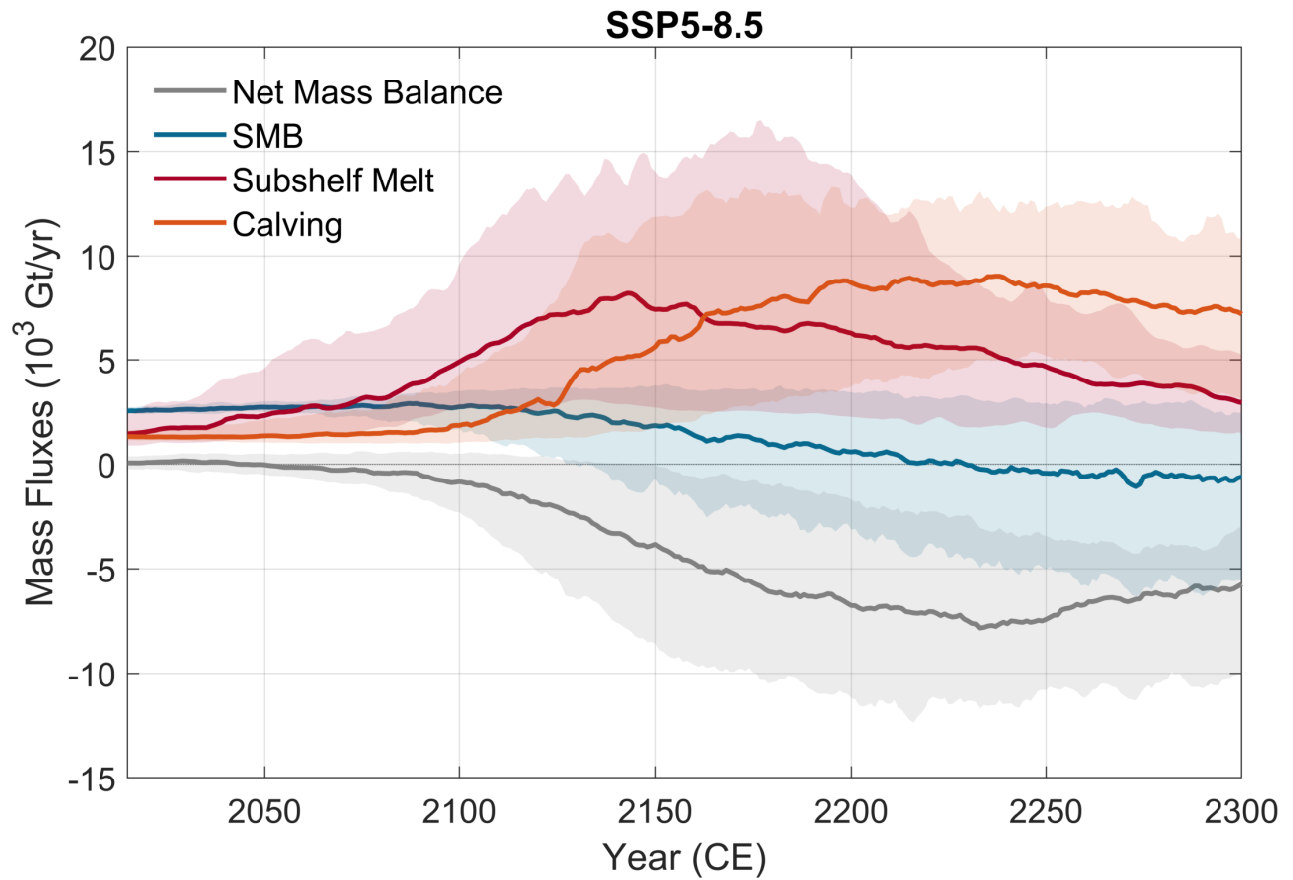
Figure S5: **Calibrated probabilistic projections of the Antarctic ice sheet mass balance components until the year 2300 CE under SSP5-8.5 when accounting for ice shelf hydrofracturing**. Solid lines and shaded regions show the median and 5-95% probability intervals (N=100), with 5-year running average applied. Positive SMB fluxes represent mass gains while positive sub-shelf melt and calving fluxes represent mass losses. Note that the ice-sheet net mass balance does not represent the sum of all mass balance components but instead considers changes in volume above flotation and may therefore be interpreted as the rate of mass change contributing to sea-level rise.
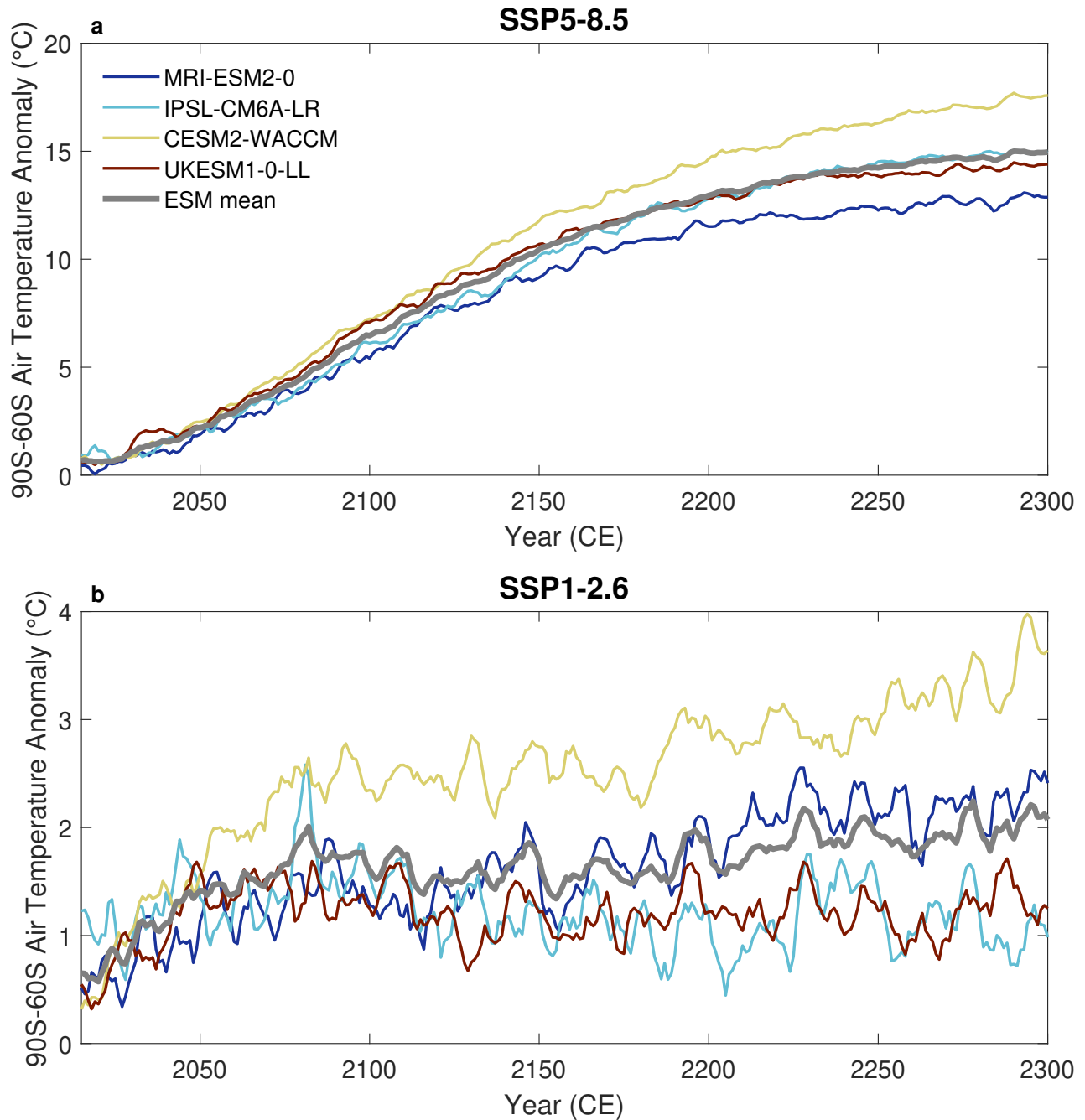
Figure S6: **Time series of the regional (between 90–60°S) annual near-surface air temperature anomaly (°C) projected by the four GCMs from the sixth phase of the Coupled Model Intercomparison Project (CMIP6) used in this study under SSP1-2.6 (a) and SSP5-8.5 (b) compared to the 1995-2014 reference period.** The thick grey lines represent the mean annual warming from the four GCMs. A running average of 5 years was applied for better readability.

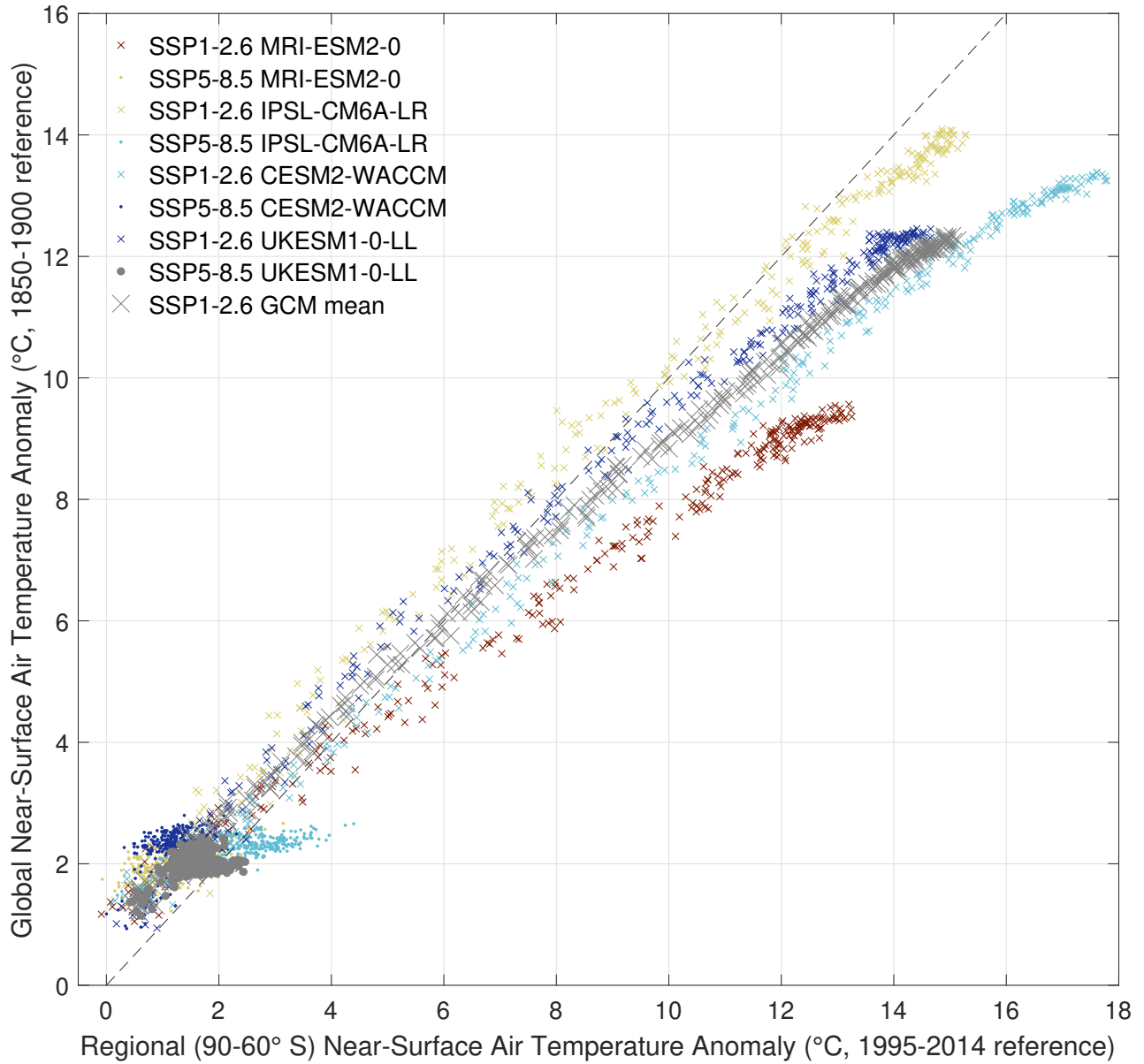Figure S7: **Comparison between the Antarctic regional (between 90–60°S) annual near-surface air temperature anomaly (°C) compared to present-day (1995-2014 reference period) with the annual pre-industrial (relative to the 1850-1900 reference period) near-surface warming projected by the four GCMs from the sixth phase of the Coupled Model Intercomparison Project (CMIP6) used in this study.** The dashed line is the identity line.

a Modelled Surface Velocity (m yr⁻¹)

b Observed Surface Velocity (m yr⁻¹)

c Surface Velocity Misfit (m yr⁻¹)

d

RMSE = 101.6 m yr⁻¹

e Ice Thickness Misfit (m)
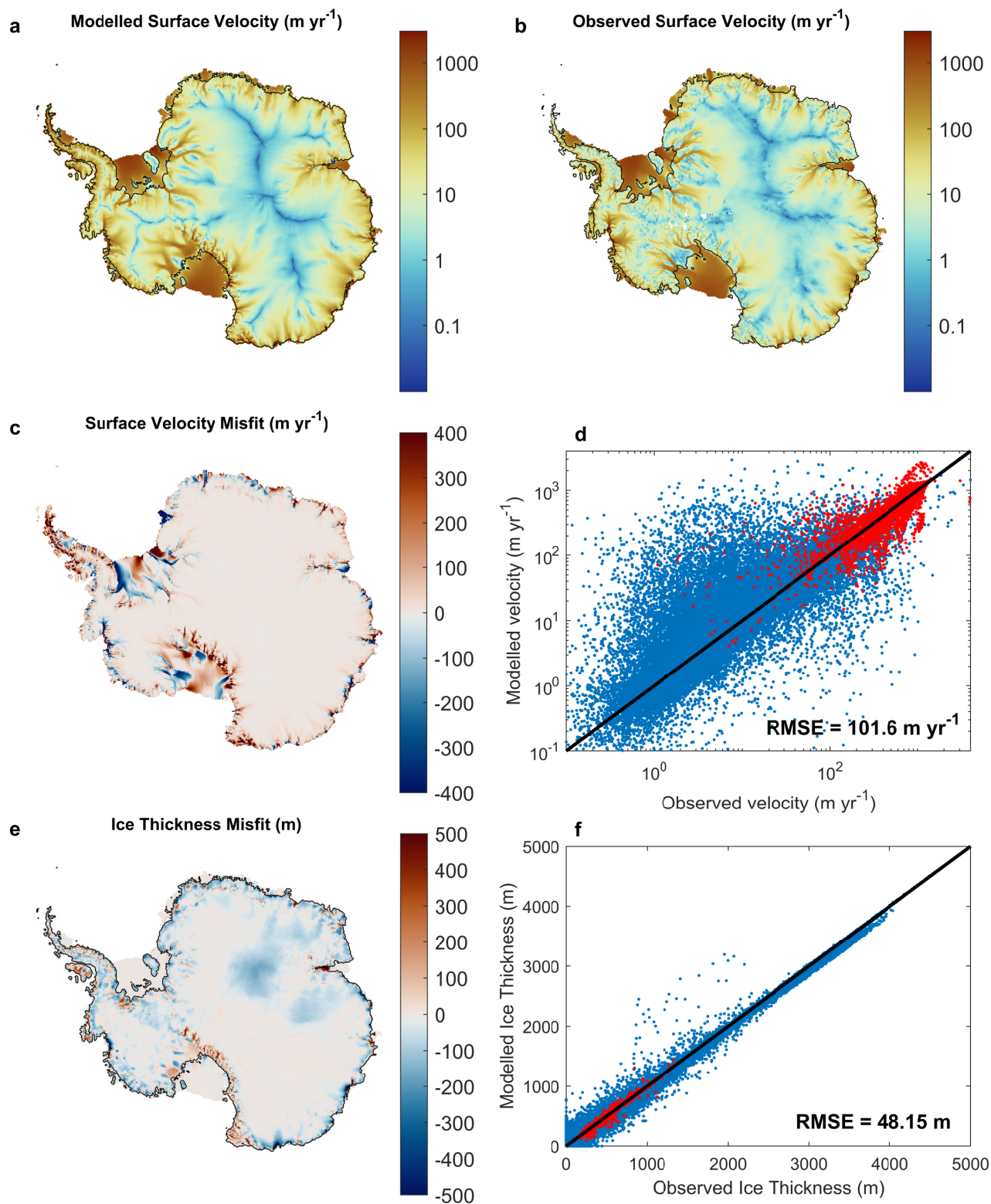
f

RMSE = 48.15 m

Figure S8: **Ice-sheet initial state obtained with the 1995-2014 atmospheric climatology from MARv3.11 (Kittel et al., 2021) adjusted with a 1945-1955 anomaly from NorESM1-M.** Shown is a comparison of the ice sheet thickness and ice velocities as modelled by Kori in the year 1950 (i.e., after the initialisation) to observed ice sheet thickness (Morlighem et al., 2019, Bedmachine;) and velocities (Rignot et al., 2011), using the atmospheric climatology derived from MAR adjusted with a 1945-1955 anomaly derived from NorESM1-M. Modelled and observed surface velocities are illustrated in (a) and (b). Modelled minus observed ice velocity and thickness are given in (c) and (e) with the modelled grounding line in black, respectively, while point-by-point scatter plots for comparison of modelled and observed ice-sheet (blue) and ice-shelf (red) velocities and thicknesses are shown in (d) and (f).

8
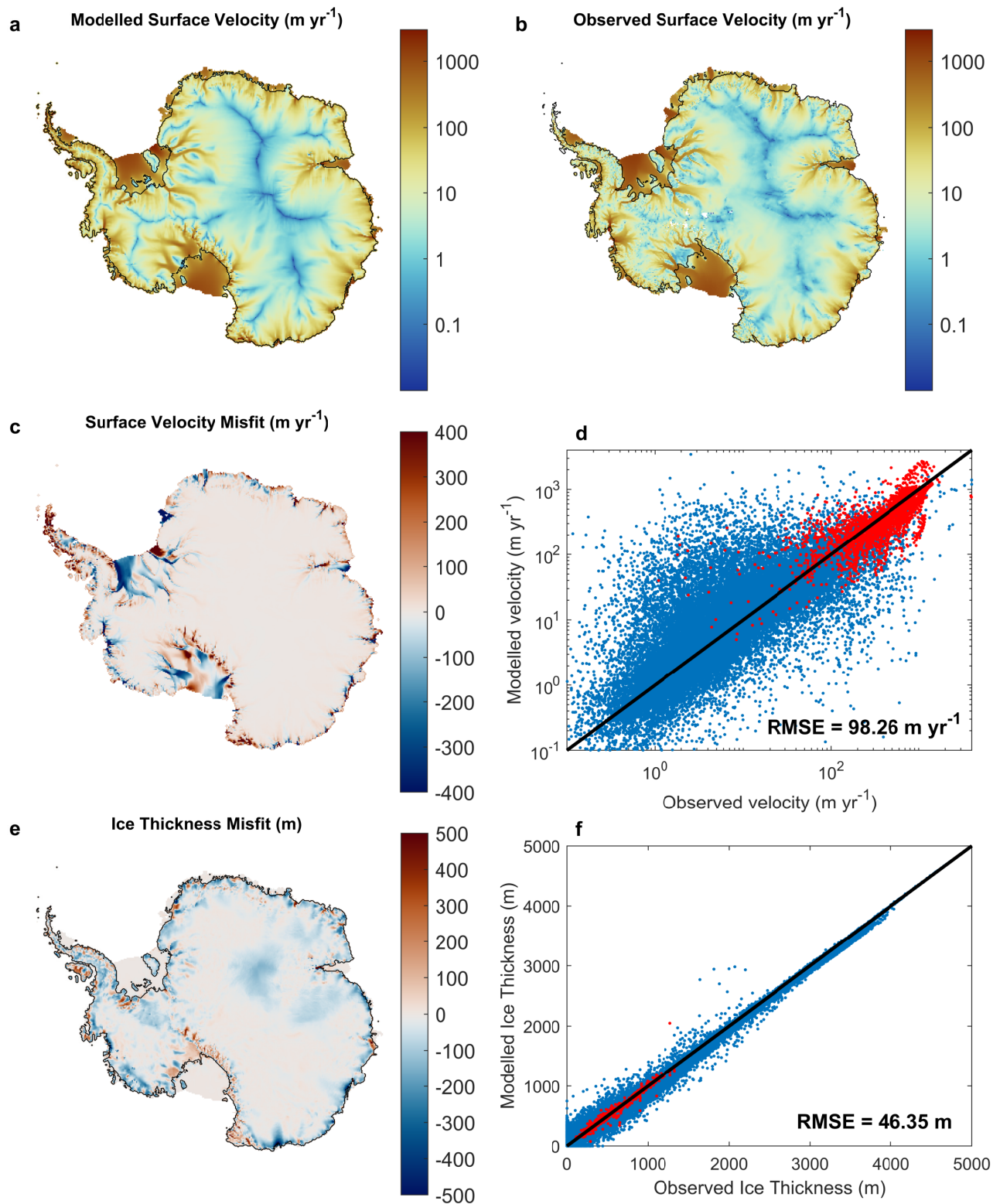
Figure S9: **Ice-sheet initial state obtained with the 1995-2014 atmospheric climatology from RACMO2.3p2 (van Wessem et al., 2018) adjusted with a 1945-1955 anomaly from NorESM1-M.** Shown is a comparison of the ice sheet thickness and ice velocities as modelled by Kori in the year 1950 (i.e., after the initialisation) to observed ice sheet thickness (Morlighem et al., 2019, Bedmachine;) and velocities (Rignot et al., 2011), using the atmospheric climatology derived from RACMO adjusted with a 1945-1955 anomaly derived from NorESM1-M. Modelled and observed surface velocities are illustrated in (a) and (b). Modelled minus observed ice velocity and thickness are given in (c) and (e) with the modelled grounding line in black, respectively, while point-by-point scatter plots for comparison of modelled and observed ice-sheet (blue) and ice-shelf (red) velocities and thicknesses are shown in (d) and (f).
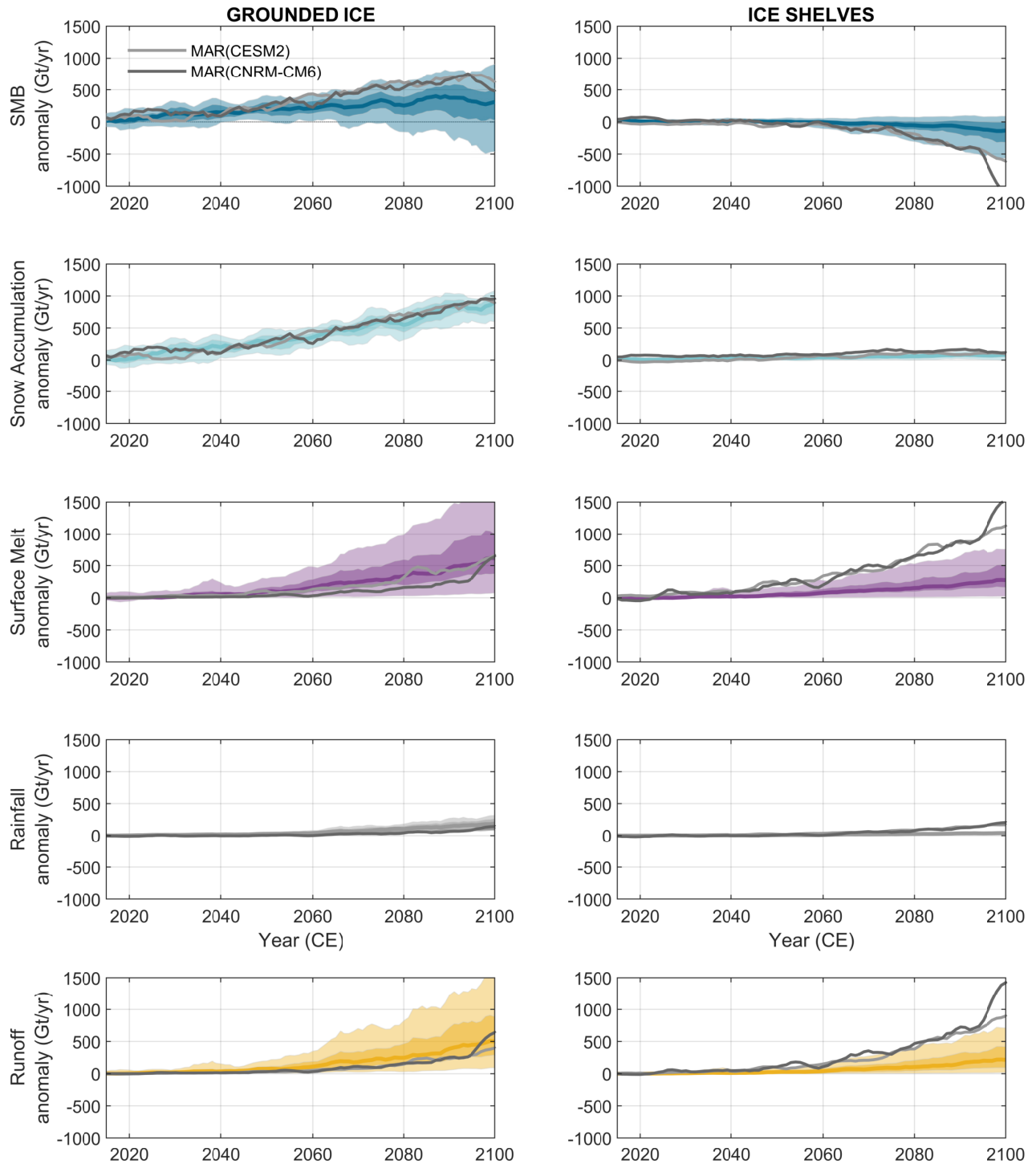
9

Figure S10: **Evolution of the calibrated probabilistic projections of the Antarctic integrated main surface mass balance components until the year 2100 CE over the grounded ice sheet (a,c,e,g) and the ice shelves (b,d,f,h) compared with projections from MAR.** Evolution of the ensemble projected anomalies in total surface mass balance (a—b), snow accumulation (c—d), surface runoff (e—f), and rain precipitation (g—h) for the 2015-2100 period under the shared socio-economic pathway (SSP) 5-8.5 over the grounded ice sheet (left) and the ice shelves (right). Colored solid lines and shaded regions show the median, 25-75%, and 5-95% probability intervals (N=100 per SSP scenario), with 5-year smoothing applied. Grey solid lines show the time series of the integrated annual SMB components simulated by MAR forced by CNRM-CM6-1 (dark grey), and CESM2 (light grey). Note that positive SMB, snow accumulation and rainfall fluxes represent mass gains while positive surface melt and runoff fluxes represent mass losses.
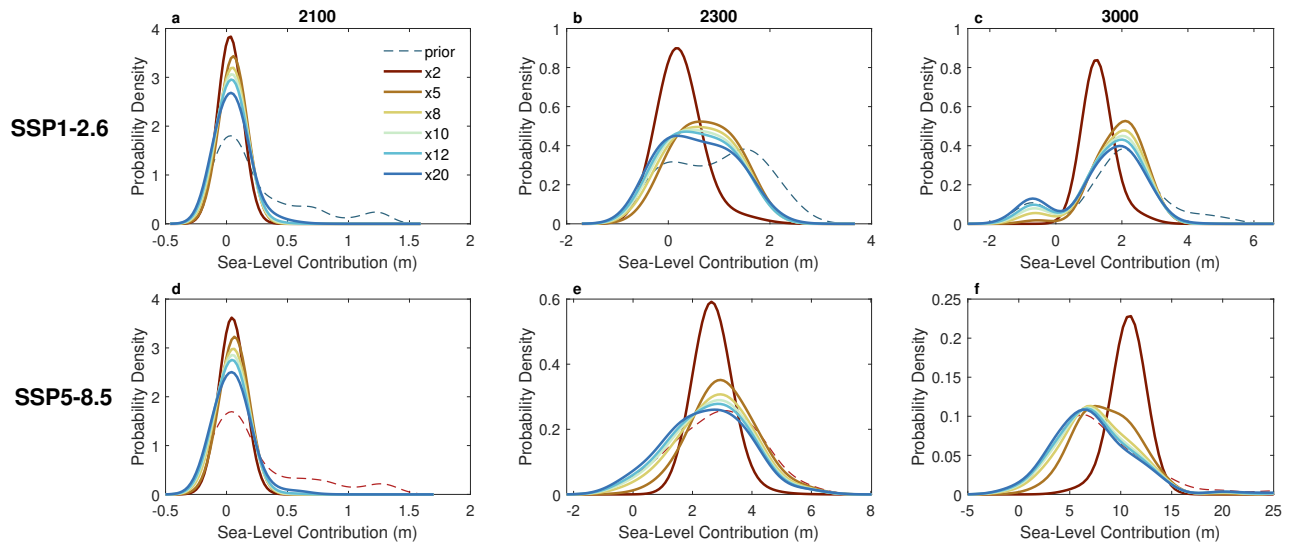
Figure S11: **Prior (dashed lines) and posterior (plain lines) probability density functions of the Antarctic sea-level contribution under SSP1-2.6 (a–c) and SSP5-8.5 (d–f) by 2100 (a,d), 2300 (b,e), and 3000 (c,f).** Different values for the structural error have been tested by multiplying the observational error by 2, 5, 8, 10, 12, or 20.

Scenario	Year	Distribution	Quantiles		
			5%	50%	95%
SSP1-2.6					
	2100	Prior	-0.1096	0.1075	1.1832
		Posterior, $\sigma_i^{\mathrm{mod}} = 8\sigma_i^{\mathrm{obs}}$	-0.0666	0.0588	0.1467
		Posterior, $\sigma_i^{\mathrm{mod}} = 10\sigma_i^{\mathrm{obs}}$	-0.0831	0.0588	0.1467
		Posterior, $\sigma_i^{\mathrm{mod}} = 12\sigma_i^{\mathrm{obs}}$	-0.0886	0.0588	0.1482
	2300	Prior	-0.2990	1.0693	2.1816
		Posterior, $\sigma_i^{\mathrm{mod}} = 8\sigma_i^{\mathrm{obs}}$	-0.1746	0.6268	1.5618
		Posterior, $\sigma_i^{\mathrm{mod}} = 10\sigma_i^{\mathrm{obs}}$	-0.2602	0.6175	1.5618
		Posterior, $\sigma_i^{\mathrm{mod}} = 12\sigma_i^{\mathrm{obs}}$	-0.2803	0.5918	1.5618
	3000	Prior	-0.8058	1.9755	4.2250
		Posterior, $\sigma_i^{\mathrm{mod}} = 8\sigma_i^{\mathrm{obs}}$	-0.5617	1.9072	2.9042
		Posterior, $\sigma_i^{\mathrm{mod}} = 10\sigma_i^{\mathrm{obs}}$	-0.7336	1.8490	2.9042
		Posterior, $\sigma_i^{\mathrm{mod}} = 12\sigma_i^{\mathrm{obs}}$	-0.7441	1.8466	2.9042
SSP5-8.5					
	2100	Prior	-0.1246	0.1172	1.2451
		Posterior, $\sigma_i^{\mathrm{mod}} = 8\sigma_i^{\mathrm{obs}}$	-0.0839	0.0547	0.1452
		Posterior, $\sigma_i^{\mathrm{mod}} = 10\sigma_i^{\mathrm{obs}}$	-0.1031	0.0547	0.1562
		Posterior, $\sigma_i^{\mathrm{mod}} = 12\sigma_i^{\mathrm{obs}}$	-0.1092	0.0425	0.1576
	2300	Prior	0.4170	2.8576	4.7343
		Posterior, $\sigma_i^{\mathrm{mod}} = 8\sigma_i^{\mathrm{obs}}$	0.6981	2.9230	4.5148
		Posterior, $\sigma_i^{\mathrm{mod}} = 10\sigma_i^{\mathrm{obs}}$	0.4604	2.7388	4.5148
		Posterior, $\sigma_i^{\mathrm{mod}} = 12\sigma_i^{\mathrm{obs}}$	0.4604	2.6216	4.2814
	3000	Prior	2.4023	7.1217	16.2939
		Posterior, $\sigma_i^{\mathrm{mod}} = 8\sigma_i^{\mathrm{obs}}$	2.4023	7.2441	13.4660
		Posterior, $\sigma_i^{\mathrm{mod}} = 10\sigma_i^{\mathrm{obs}}$	2.4023	6.9523	13.4660
		Posterior, $\sigma_i^{\mathrm{mod}} = 12\sigma_i^{\mathrm{obs}}$	2.4023	6.9523	13.4660

Table S1: **Quantiles from the prior and posterior distributions of sea-level contribution (mm SLE) by years 2100, 2300, and 3000 relative to 2015**.
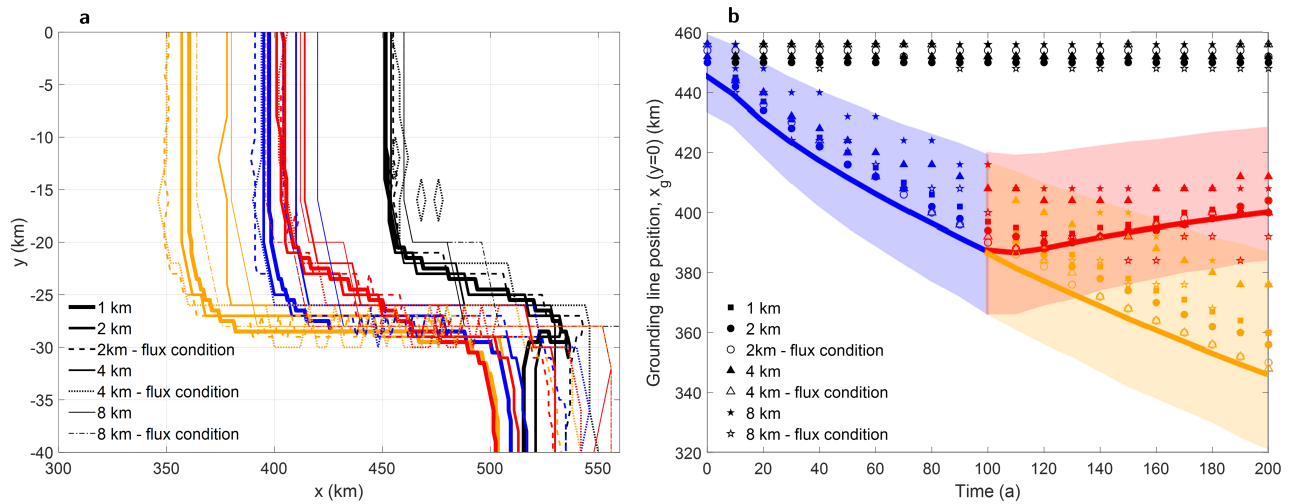
Figure S12: **Grounding-line positions for the MISMIP+ Ice 1 experiments with Kori-ULB**. (a) Final grounding-line positions at the end of each step of the Ice 1 experiments within the MISMIP+ ice stream domain, which is a rectangular domain spanning 640 km in the x direction and 80 km in the y direction. Ice flows in a direction roughly parallel to the x axis (with a mirror symmetry in the lateral center of the ice stream – midchannel position is at $y = 0$). (b) Midchannel grounding line positions plotted against time for the Ice 1 experiments. A retrograde bed slope is observed between $x = 400$ and $x = 500$ km. All experiments are run at different spatial resolutions (1, 2, 4 and 8 km), and with (at 2, 4 and 8-km resolution only) and without using a flux condition to determine grounding-line migrations. Black curves and symbols correspond to the Ice 0 (control) experiment. Blue curves and symbols correspond to the Ice1r experiment (melt-induced retreat). Red curves and symbols correspond to the Ice1ra experiment (no melting readvance). Finally, yellow curves and symbols correspond to the Ice1rr experiment (further melt-induced retreat). More information on the experiments setup and the domain are provided in Cornford et al. (2020). Lines and shaded regions in (b) show the envelopes for the 'main subset' of MISMIP+ models, copied from Cornford et al. (2020, their Fig. 7a).
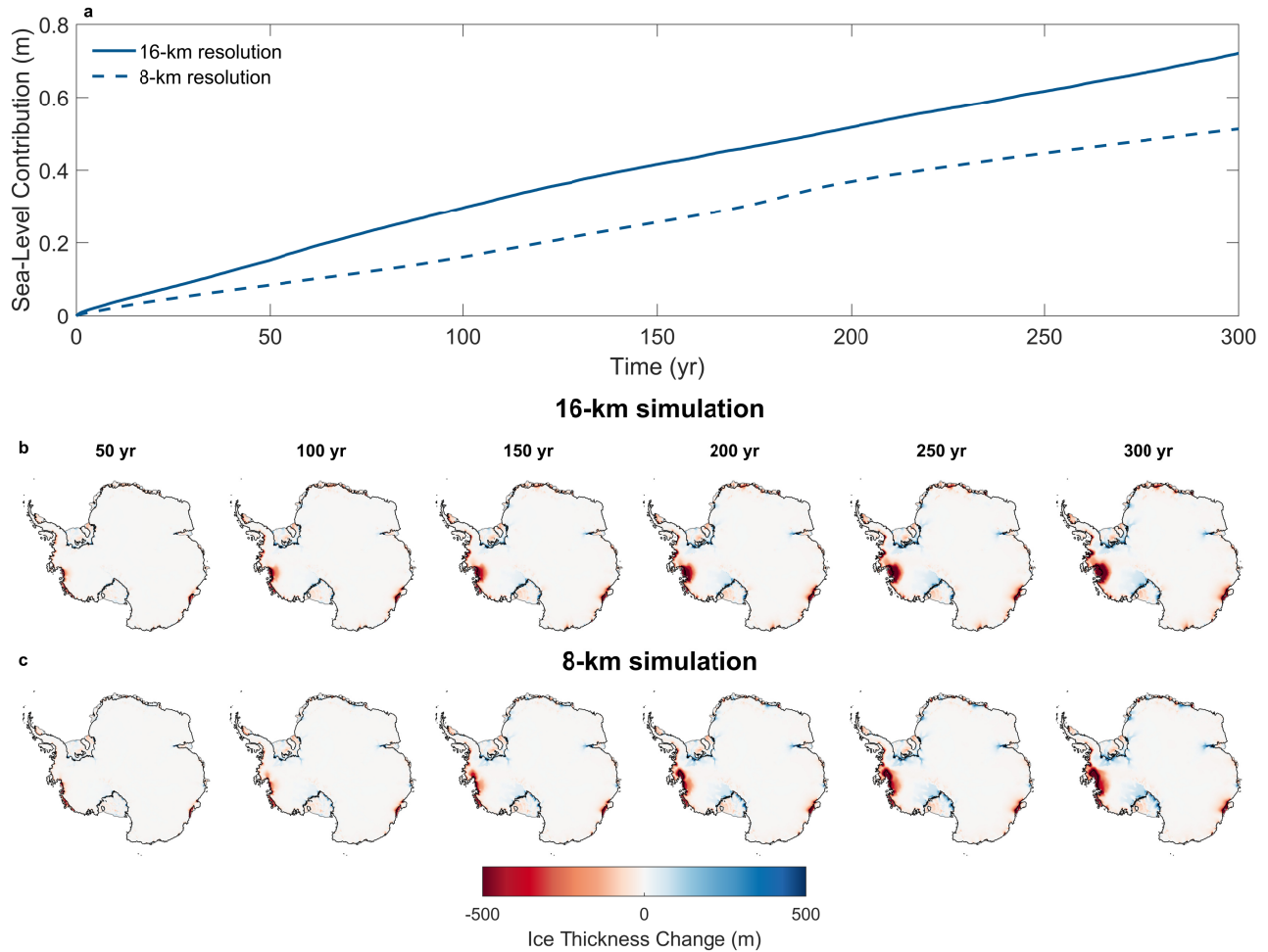
Figure S13: **Resolution dependence test: a comparative analysis between 16-km (used in this study) and 8-km resolution 300-yr simulations under constant present-day conditions**. Climatologies for present-day atmospheric and oceanic conditions were derived from RACMOv2.3p2 (van Wessem et al., 2018) and Schmidtko et al. (2014), respectively. Sub-shelf melt rates are computed using the PICO model (Reese et al., 2018) with an effective ice-ocean heat flux parameter $\gamma_T^\star$ set to the upper limit of our parameter space (10×10^{-5}). (a) Evolution of the contribution of the Antarctic ice sheet to global mean sea-level rise over time (in meters). (b-c) Ice thickness changes at various points in time during the simulations for the 16-km (b) and 8-km (c) resolutions, respectively. Grounding line and calving front positions are represented by black and grey lines, respectively. The finer 8-km resolution simulation shows Pine Island Glacier retreating more rapidly, while Thwaites Glacier retreats at a slower pace. We attribute these differences to differences in bedrock topography and initial state configurations.

14

References

Cornford, S. L., Seroussi, H., Asay-Davis, X. S., Gudmundsson, G. H., Arthern, R., Borstad, C., Christmann, J., Dias dos Santos, T., Feldmann, J., Goldberg, D., Hoffman, M. J., Humbert, A., Kleiner, T., Leguy, G., Lipscomb, W. H., Merino, N., Durand, G., Morlighem, M., Pollard, D., Rückamp, M., Williams, C. R., and Yu, H. (2020). Results of the third Marine Ice Sheet Model Intercomparison Project (MISMIP+). *The Cryosphere*, 14(7):2283–2301.

Kittel, C., Amory, C., Agosta, C., Jourdain, N. C., Hofer, S., Delhasse, A., Doutreloup, S., Huot, P.-V., Lang, C., Fichefet, T., and Fettweis, X. (2021). Diverging future surface mass balance between the antarctic ice shelves and grounded ice sheet. *The Cryosphere*, 15(3):1215–1236.

Morlighem, M., Rignot, E., Binder, T., Blankenship, D., Drews, R., Eagles, G., Eisen, O., Ferraccioli, F., Forsberg, R., Fretwell, P., Goel, V., Greenbaum, J. S., Gudmundsson, H., Guo, J., Helm, V., Hofstede, C., Howat, I., Humbert, A., Jokat, W., Karlsson, N. B., Lee, W. S., Matsuoka, K., Millan, R., Mouginot, J., Paden, J., Pattyn, F., Roberts, J., Rosier, S., Ruppel, A., Seroussi, H., and Smith, E. C. (2019). Deep glacial troughs and stabilizing ridges unveiled beneath the margins of the Antarctic ice sheet. *Nature Geoscience*.

Reese, R., Albrecht, T., Mengel, M., Asay-Davis, X., and Winkelmann, R. (2018). Antarctic sub-shelf melt rates via pico. *The Cryosphere*, 12(6):1969–1985.

Rignot, E., Mouginot, J., and Scheuchl, B. (2011). Ice flow of the antarctic ice sheet. *Science*, 333(6048):1427–1430.

Schmidtko, S., Heywood, K. J., Thompson, A. F., and Aoki, S. (2014). Multidecadal warming of Antarctic waters. *Science*, 346(6214):1227–1231.

van Wessem, J. M., van de Berg, W. J., Noël, B. P. Y., van Meijgaard, E., Amory, C., Birnbaum, G., Jakobs, C. L., Krüger, K., Lenaerts, J. T. M., Lhermitte, S., Ligtenberg, S. R. M., Medley, B., Reijmer, C. H., van Tricht, K., Trusel, L. D., van Ulft, L. H., Wouters, B., Wuite, J., and van den Broeke, M. R. (2018). Modelling the climate and surface mass balance of polar ice sheets using racmo2 – part 2: Antarctica (1979–2016). *The Cryosphere*, 12(4):1479–1498.